Acta Materialia 286 (2025) 120709

Contents lists available at ScienceDirect

Acta Materialia

journal homepage: www.elsevier.com/locate/actamat

Superimpositional design of crystallographic textures and macroscopic shapes via metal additive manufacturing—Game-change in component design

Takuya Ishimoto [a,b], Naotaka Morita [a], Ryosuke Ozasa [a,c], Aira Matsugaki [a,c], Ozkan Gokcekaya [a,c], Shota Higashino [d], Masakazu Tane [a,c], Tsuyoshi Mayama [e], Ken Cho [a,c], Hiroyuki Y. Yasuda [a,c], Masayuki Okugawa [a,c], Yuichiro Koizumi [a,c], Masato Yoshiya [a,c], Daisuke Egusa [f], Taisuke Sasaki [g], Eiji Abe [f], Hajime Kimizuka [h], Naoko Ikeo [i], Takayoshi Nakano [a,c,*]

[a] Division of Materials and Manufacturing Science, Graduate School of Engineering, The University of Osaka, 2-1, Yamadaoka, Suita, Osaka 565-0871, Japan
[b] Aluminium Research Center, University of Toyama, 3190, Gofuku, Toyama, Toyama 930-8555, Japan
[c] Anisotropic Design & Additive Manufacturing Research Center, The University of Osaka, 2-1, Yamadaoka, Suita, Osaka 565-0871, Japan
[d] Graduate School of Engineering, Osaka Metropolitan University, 1-1, Gakuen-cho, Nakaku, Sakai, Osaka 599-8531, Japan
[e] Department of Materials Science and Engineering, Kumamoto University, 2-39-1, Kurokami, Chuo-ku, Kumamoto, Kumamoto 860-8555, Japan
[f] Department of Materials Science and Engineering, The University of Tokyo, 7-3-1, Hongo, Bunkyo-ku, Tokyo 113-8656, Japan
[g] National Institute for Materials Science, 1-2-1 Sengen, Tsukuba, Ibaraki 305-0047, Japan
[h] Department of Materials Design Innovation Engineering, Graduate School of Engineering, Nagoya University, Furo-cho, Chikusa-ku, Nagoya, Aichi 464-8603, Japan
[i] Department of Mechanical Engineering, Graduate School of Engineering, Kobe University, 1-1, Rokkodai-cho, Nada-ku, Kobe, Hyogo 657-8501, Japan

ARTICLE INFO

Keywords:
Laser powder bed fusion
Shape anisotropy
Crystallographic orientation
Superimposition
3D puzzle
Young's modulus

ABSTRACT

This study demonstrates the control of the crystalline orientation through metal additive manufacturing, enabling the development of component design guidelines that incorporate the inherent anisotropy of the mechanical properties (e.g., Young's modulus) in crystalline materials. We, for the first time, successfully fabricated a <111>//build direction (BD)-oriented single-crystalline-like texture in an alloy with a cubic crystal structure via laser powder bed fusion (LPBF) and completed a series of three single-crystalline-like microstructures with <001>, <011>, and <111>//BD orientations in a single material. The <001> and <111> directions exhibited the lowest and highest Young's moduli, respectively, demonstrating a wide range of control over the anisotropy of the mechanical properties of the product. To achieve a <111>//BD-oriented single-crystalline-like texture, a novel three-layer cyclic strategy of "uni"directional laser scanning at 120° angular intervals was developed by considering the easy growth direction and crystal symmetry. To the best of our knowledge, no previous study has reported this unique strategy. By superimposing the realized <111> orientation and shape-based anisotropy, products exhibiting high Young's modulus anisotropy, which cannot be expressed by shape and texture alone, were obtained via the LPBF single process. This achievement holds promise for the realization of a new component design guideline that integrates texture (mechanical properties) design for each internal location—modifiable through scanning strategies—with traditional shape optimization techniques typically used in computer-aided design. This approach enables tailored mechanical performance through optimized design strategies.

1. Introduction

Additive manufacturing (AM) is being increasingly adopted in a wide range of industries, such as aerospace, motor vehicles, medicine, military, electronics, and architecture [1], primarily as a technology that enables the creation of products with complex three-dimensional (3D)

* Corresponding author at: Division of Materials and Manufacturing Science, Graduate School of Engineering, The University of Osaka, 2-1, Yamadaoka, Suita, Osaka 565-0871, Japan.
E-mail address: nakano@mat.eng.osaka-u.ac.jp (T. Nakano).

https://doi.org/10.1016/j.actamat.2025.120709
Received 4 September 2024; Received in revised form 2 December 2024; Accepted 1 January 2025
Available online 2 January 2025

shapes and a high degree of freedom. In particular, powder bed fusion (PBF)—a representative AM process—is capable of producing complex-shaped products with high shape accuracy owing to fine raw powder and highly focused heat source.

In PBF, products are manufactured by stacking tiny melt pools generated by focused beams as a unit, and achieving a specific crystallographic texture inside the product has recently become possible by adjusting the melt pool shape [2–7]. The formation and further control of crystallographic texture is known to be extremely effective in improving the mechanical functionality of products. For example, in turbine blades used at high temperatures, single crystallization of Ni-based alloys significantly suppresses creep deformation due to grain boundary sliding at high temperatures and increases the high-temperature strength [8]. In another example, single crystallization of metastable β-Ti alloy with body-centered cubic (BCC) structure for bone implants produces low Young's modulus along <001> [9,10], and single-crystalline β-Ti implants are expected to be next-generation medical devices [11] that suppress bone degradation due to strain shielding [12]. In particular, crystallographic texture formation can selectively enhance the mechanical functionality of metallic parts in anisotropic loading environments by imparting anisotropy to intrinsic mechanical properties. By superimposing internal texture control on the shape design—which is the original strength of AM—a new design can be created that is more flexible, versatile, and effective than the conventional design, which has a lighter weight and higher specific strength for a given stress distribution.

In this study, we attempted to combine shape and crystallographic texture to realize flexible mechanical functions, particularly variations in the Young's modulus from isotropic to highly anisotropic. We hypothesized that the superposition of shape and texture would enable the expression of a large anisotropy that cannot be realized by either alone.

In 2017, we reported the successful formation of single-crystal-like textures using laser PBF (LPBF) and that the scanning strategy (SS) referring to combination of laser scanning directions between layers changes the orientation direction [13,14]. As described in detail later, we obtained two types of single-crystalline-like textures with <001> or <011> preferentially oriented in the build direction (BD), which were controlled using general SSs. The <111> orientation is known to exhibit the highest Young's modulus in many alloys that exhibit cubic crystal structures [9,15–18]. In addition, materials with cubic crystal structures have the lowest Schmid factor, and thus, the maximum yield strength when loaded along the <111> direction. Thus, the realization of the <111> orientation is expected to significantly expand the range of control over the anisotropy of the mechanical properties. However, a single-crystalline-like texture control with <111>//BD orientation has not yet been realized. In this study, we clarify the formation mechanism of <001>//BD- and <011>//BD-oriented single-crystalline-like textures that have been previously achieved. Based on these findings, we propose and demonstrate a new SS that can realize <111>//BD single-crystalline-like texture. Furthermore, we aim to develop products expressing large Young's modulus anisotropy, which is possible only by the superposition of shape and texture, by fully utilizing the <111> orientation with the highest Young's modulus. We used a Ti–15Mo–5Zr–3Al alloy with a BCC structure that exhibits large Young's modulus anisotropy, with higher Young's moduli (E) in the order $E_{111} > E_{011} = E_{211} > E_{001}$ [10], as shown in Supplementary Fig. S1.

2. Laser scanning strategy for <111>//BD single-crystalline-like texture formation: scanning path selection based on crystal symmetry

The choice of laser SS governs the control and creation of crystallographic orientation in the products [13,19–21]. Thus far, we have achieved single-crystalline-like texture for <001>//BD and <011>//BD [13]. To realize <111>//BD single-crystalline-like texture, we elaborated the formation mechanism of two textures that have been successfully fabricated. We have reached the insight that the symmetry of the laser SS, tuned to the symmetry of the crystal and crystallographic easy-growth direction (<001> for metallic materials with cubic structure [22]), is the key to forming single-crystalline-like textures.

Fig. 1(a–c) show the 3D view of the targeted orientation and Fig. 1(d–f) depict the projection of the targeted texture as viewed from BD when <001>//BD, <011>//BD, and <111>//BD single crystals are formed. The symmetries of the crystal as viewed from BD are four-fold (Fig. 1(d)), two-fold (Fig. 1(e)), and three-fold rotational symmetry (Fig. 1(f)), and the rotational axes are <001>, <011>, and <111>, respectively. These crystallographic textures are denoted as $\{001\}_z$ $<100>_x$, $\{011\}_z$ $<100>_x$, and $\{111\}_z$ $<2\overline{11}>_x$, respectively, using the directions in which they should be preferentially oriented in the BD (z-) and x-directions Fig. 1(a–c).

The laser SSs for achieving <001>//BD and <011>//BD single-crystalline-like textures include ±XY_SS, where the laser is bidirectionally scanned alternately along the x- and y-axes for each layer (Fig. 1(j)), and ±X_SS, in which the laser is bidirectionally scanned along the x-axis for each layer (Fig. 1(k)), as previously reported [13]. To distinguish them from the newly developed SS described in the next paragraph, "±" is added to indicate "bidirectional" scan. Separating the laser path elements of these SSs, Fig. 1(g, h) show that they match the crystal symmetry illustrated in Fig. 1(d, e).

Based on these geometrical insights, we hypothesized that a three-directional laser scanning path with angles rotating every 120°, as shown in Fig. 1(i), yields <111>//BD single-crystalline-like texture. Fig. 1(l) reflects this in the SS, which is a novel three-layer cyclic strategy of "uni"directional laser scanning at 120° intervals instead of the conventional bidirectional laser scanning. This novel SS was named +120°Rot_SS. The "+" in the prefix means that the laser scanning is unidirectional.

3. Experimental procedures

3.1. LPBF fabrication

An ingot with a nominal composition of Ti–15Mo–5Zr–3Al (wt.%) was used as the starting material. The powder for LPBF fabrication was prepared using Ar gas atomization (Osaka Titanium Technologies Co., Ltd., Japan). The obtained powder particles were spherical (Supplementary Fig. S2(a)), with a size distribution of D_{10} = 10.0 μm, D_{50} = 31.6 μm, and D_{90} = 50.3 μm (Supplementary Fig. S2(b)), measured using a particle size analyzer (Mastersizer 3000E, Malvern Panalytical, UK).

Rectangular specimens with a bottom dimension of 5 mm × 5 mm were manufactured using an LPBF apparatus (EOS M 290, EOS, Germany) equipped with a 400 W Yb fiber laser. The laser diameter was tuned to 100 μm. The fabrication was performed in an Ar atmosphere. By manufacturing products under various laser conditions [13,20], suitable scan process parameters for the formation of single-crystalline-like texture were optimized. The scan process parameters, i.e., the laser power, scanning speed, layer thickness, and hatch spacing were set to 360 W, 1200 mm/s, 60 μm, and 100 μm, respectively. The cross-sectional shape of the melt pool under these conditions is shown in Supplementary Fig. S3. The melt pool depth reached approximately 300 μm; however, almost no gas porosity entrapment occurred, which is often a problem in the keyhole mode melting, suggesting that the manufacturing process was operated in the transition mode [23]. Fabrication was carried out using +120°Rot_SS (Fig. 1(l)) for <111>//BD single crystal, along with ±XY_SS (Fig. 1(j)), ±X_SS (Fig. 1(k)), and ±67°Rot_SS (generally adopted in many studies) for <001>//BD, <011>//BD, and crystallographically random polycrystalline textures, respectively. For randomly oriented polycrystal, to eliminate the effect of preferential grain elongation along the BD on the Young's moduli in the orthogonal three directions of the specimens, the specimens were fabricated by placing one of their diagonals parallel to

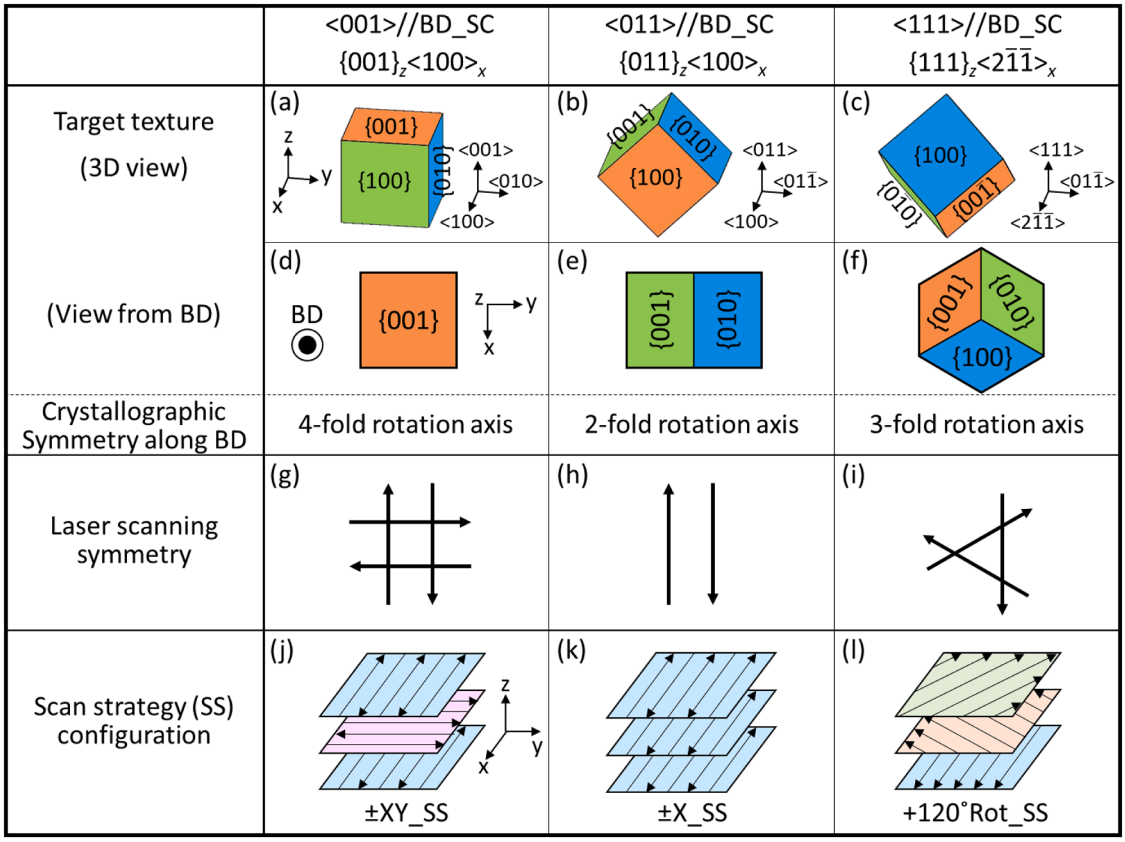

Fig. 1. Relationship between crystal orientation-dependent rotational symmetry and scanning strategy. (a–c) 3D view of targeted crystallographic textures, (d–f) projection of the targeted textures viewed from build direction (BD), (g–i) laser path symmetry that matches the crystal symmetry, and (j–l) schematic of the combination of laser scanning paths and directions for each layer that represents the laser scan strategy. SC: single crystal.

the BD (Supplementary Fig. S4). Specimens with other textures were produced by placing one side parallel to the BD.

3.2. Microstructural observation

The microstructures of the fabricated samples were examined using optical microscopy (OM; BX60, Olympus, Japan) and field-emission

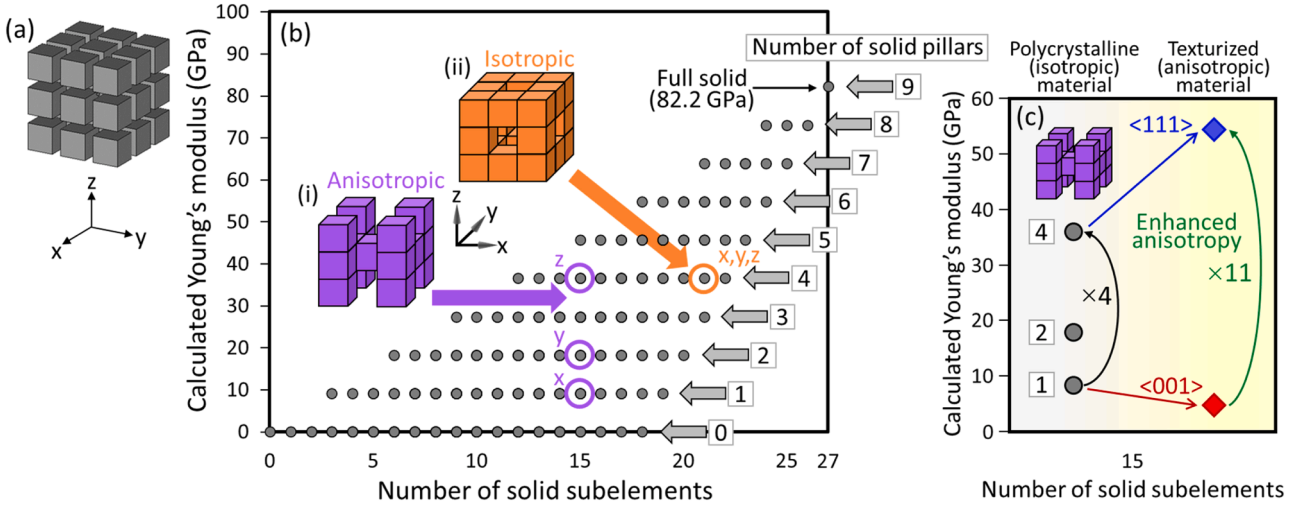

Fig. 2. (a) Framework of the structure consisting of 27 small cubic subelements (3 × 3 × 3 configuration) for designing isotropic/anisotropic Young's modulus. (b) Possible Young's modulus variations as functions of the number of solid cube subelements and the number of solid pillars (three sequential subelements) when the element is composed of polycrystals, calculated using the Reuss and Voigt rules. The product (i) with one, two, and four pillars depending on the direction exhibits different values in the three orthogonal axes (structurally anisotropic), while the product (ii) with four pillars in all directions shows the same moduli (structurally isotropic). (c) Enhancement of Young's modulus anisotropy when crystallographic texture (single crystal) is introduced for the anisotropic structure shown in purple. To maximize the overall Young's modulus anisotropy of the product, <001> should be oriented parallel to the direction of one pillar (*x*-axis) and <111> parallel to the direction of four pillars (*z*-axis). These configurations correspond to models D and F in Fig. 5 and can actually be manufactured.

scanning electron microscopy (FE-SEM; JIB-4610F, JEOL, Japan). The surface of the sample was mechanically polished using emery papers. Subsequently, final polishing was conducted with colloidal silica. The specimens were etched in a solution consisting of 2 % HNO_3, 1 % HF, and 97 % H_2O for approximately 1 min with ultrasonic vibration at room temperature to accurately observe the melt-pool traces and solidification microstructure. The crystallographic texture analysis was conducted using an electron backscatter diffraction (EBSD) system (NordlysMax^3, Oxford Instruments, UK) mounted on the FE-SEM system. The software used for data collection and data processing were Aztec (Oxford Instruments, UK) and Channel 5 (Oxford Instruments, UK), respectively.

3.3. Creation of "3D puzzle" for designing anisotropy/isotropy in Young's modulus via superimposition of product shape and crystallographic texture

For the design of isotropic/anisotropic Young's modulus, a framework of structure consisting of 27 small cubic subelements of 3 mm per side was constructed (3 × 3 × 3 arrangement) as shown in Fig. 2(a) [24]. Hence, the overall dimension of the structure was 9 mm per side. Each subelement could be assigned a solid or void. The solid refers to the portion that the raw material powder was melted and solidified by laser irradiation, and the void refers to the portion where the laser was not irradiated and the unmelted powder was removed. Young's modulus of a structure is calculated by sequentially implementing the Reuss law (rule of mixture in series: constant stress configuration) and Voigt law (rule of mixture in parallel: constant strain configuration) using the following equations, respectively [24].

$$E_{\mathrm{series,j}} = \frac{1}{\sum_{\mathrm{i}} \left(\frac{V_{\mathrm{i}}}{E_{\mathrm{i}}} \right)} \tag{1}$$

$$E_{\mathrm{structure}} = \sum\nolimits_{\mathrm{j}} E_{\mathrm{series,j}} V_{\mathrm{series,j}} \tag{2}$$

where $E_{\mathrm{series,j}}$ represents the Young's modulus of a certain series element along the loading axis; E_{i} and V_{i} denote the Young's modulus and volume fraction of each cubic subelement composing the series element, respectively; $E_{\mathrm{structure}}$ represents the apparent Young's modulus of the entire structure; and $V_{\mathrm{series,j}}$ represents the volume fraction of each series element with respect to the entire structure. A certain series element is assumed to deform independently of the other series elements.

When considering anisotropy due to shape alone, a Young's modulus of 82.2 GPa, which is the value of polycrystalline material [10], was assigned to the solid portion. Although the modulus of the void portion is 0 GPa, a sufficiently small value (0.01 GPa) was used such that Eq. (1) does not diverge. Fig. 2(b) shows the calculated Young's modulus for all configurations of solid and void portions as functions of the number of solid subelements and the resultant number of solid pillars (three sequential subelements). The number of pillars lies in a range from 0 to a maximum of nine. Thus, if the entire product is composed of isotropic polycrystalline materials (82.2 GPa), Young's modulus takes ten stepwise values between 0 and 82.2 GPa. For one product, three Young's modulus values are calculated for loads from three directions (*x*, *y*, and *z*), which are reflected in Fig. 2(b). In this study, the products with anisotropic (Fig. 2(b) inset (i)) and isotropic (Fig. 2(b) inset (ii)) geometries with respect to the *x*-, *y*-, and *z*-axes were created as model. The product in Fig. 2(b) inset (i) with 15 solid cubes shows different Young's moduli in each of the three directions, as indicated by purple circles (triaxial anisotropy); the product in Fig. 2(b) inset (ii) with 21 solid cubes shows the same Young's moduli in all three directions, as indicated by an orange circle (triaxial isotropy).

To superimpose crystallographic texture on these shapes, four types of texture, crystallographically random texture, $\{001\}_z <100>_x$, $\{011\}_z <100>_x$, and $\{111\}_z <2\bar{1}1>_x$, single-crystalline-like textures, were introduced into the product. Each texture was formed using ±67°Rot_SS (rotation strategy generally adopted in many studies), ±XY_SS, ±X_SS, and +120°Rot_SS.

For single-crystalline Ti–15Mo–5Zr–3Al, the elastic stiffness constants are $c_{11} = 142.3 \pm 1.8$ GPa, $c_{12} = 97.1 \pm 2.0$ GPa, and $c_{44} = 35.6 \pm 0.4$ GPa, and Young's modulus at each crystallographic direction calculated from these are $E_{001} = 44.4$ GPa, $E_{011} = E_{211} = 84.9$ GPa, and $E_{111} = 122$ GPa (Supplementary Fig. S1) [10]. Using these values to calculate the Young's modulus of the product using Eqs. (1) and (2), each data point in Fig. 2(b) splits vertically into three values corresponding to E_{001}, E_{011} (E_{211}), and E_{111} (Fig. 2(c)). This means that anisotropy in Young's modulus of the product can be enhanced (or reduced) by introducing single-crystalline-like texture.

3.4. Mechanical testing for determining Young's modulus

The Young's modulus of the product was measured by compression testing at an initial compressive strain rate of 0.1 %/min (AG-X, Shimadzu, Japan) ($n = 3$). Strain was analyzed using a non-contact video extensometer (TRView, Shimadzu). Resonant ultrasound spectroscopy, which enables precise analysis of elastic modulus, has recently been applied to measure Young's modulus of specimens with discontinuous geometries [25], such as those considered in this case. However, as precise measurement of the specimen geometry and inverse analysis of the elastic modulus using finite element calculations are required, we selected the aforementioned method, which is simpler and allows us to validate the concept of this study.

3.5. Statistical analyses

Quantitative results are expressed as the mean ± standard deviation. To compare data between the two groups, a two-tailed unpaired Student's *t*-test was used. To compare data among the three experimental groups, a one-way analysis of variance and post-hoc Tukey HSD multiple comparison were performed. Statistical significance was set at $P < 0.05$. SPSS version 25 software (IBM, IL, USA) for Microsoft Windows was used for all statistical analyses.

4. Results

4.1. Acquisition of <111>//BD_single-crystalline-like texture by LPBF

Fig. 3 shows inverse pole figure (IPF) maps obtained on three orthogonal planes of the product fabricated with +120°Rot_SS and the corresponding pole figures. The colors in the IPFs represent the crystallographic orientation projected normal direction of each plane. As expected, <111> is preferentially oriented in the BD (*z*-axis), and <011> and <211> are oriented in *x*- and *y*-axes, respectively, forming a single-crystalline-like $\{111\}_z <2\bar{1}1>_x$ texture.

Fig. 4 shows a SEM micrograph of a vertical cross-section of one melt pool after chemical etching and the corresponding IPF map overlaid with the traces of the melt pool edges. The IPF map is colored by the crystal orientation projected in the BD. The crystal orientation is inherited from the previously solidified parts immediately beneath and neighboring the melt pool, and evidently, the crystal orientation is maintained by epitaxial growth. SEM images show cellular-type microstructure in the transverse section of the melt pool. In this alloy, the elongation direction of the microstructure coincides with <001> [13]. As heat flow primarily occurs parallel to the direction normal to the melt pool boundary, the growth direction of the <001>-elongated microstructure is not anti-parallel to the heat flow, indicating that this microstructure is characteristic of dendrites [26]. Interestingly, the dendrites extend symmetrically toward the center on both sides of the melt pool and encounter at the center of the melt pool. Vertical lines—which correspond to the encountering points of solid–liquid

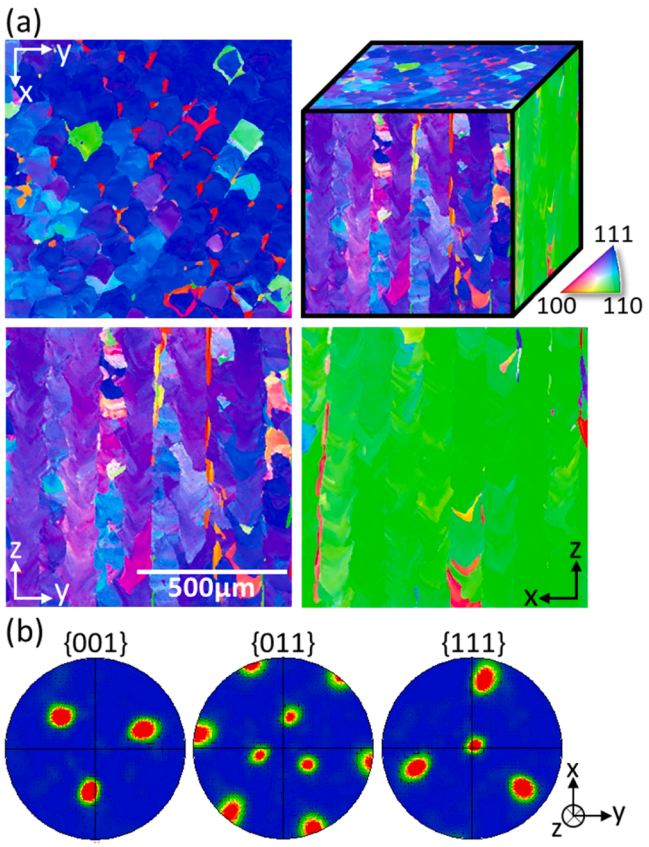

Fig. 3. (a) Inverse pole figure (IPF) maps obtained on three orthogonal planes of the product fabricated with +120°Rot_SS and (b) the corresponding pole figures for {001}, {011}, and {111}.

interfaces (hereafter referred to as "fusion boundary")—are observed at the melt pool center, as indicated by the set of facing arrows. The IPF map obtained in the same area shows a slight difference in crystallographic orientation between the left and right sides of the melt pool. However, according to the {001} pole figures shown in Fig. 4(b), the left and right sides of the melt pool have approximately the same orientation. As the direction of dendrite elongation agrees with the projected direction of one pole indicated by an arrowhead in the {001} pole figure, the direction of dendrite elongation (solid–liquid interface migration direction) is off the plane of the figure, and an oblique cross section of the dendrite is observed in Fig. 4(a). Similarly, in the *xy*-plane perpendicular to the BD, the projected major axes of dendrites and the fusion boundary at the melt pool center is observed (Supplementary Fig. S5).

4.2. Fabrication of 3D puzzle configurations and evaluation of Young's modulus

The desired <111>//BD_single-crystalline-like texture was obtained, and a 3D puzzle was created incorporating the crystallographic textures. For the two aforementioned geometry models, we created the product shown in Fig. 5. The colors on the cube elements schematically show the crystallographic orientation preferentially oriented normal to the plane. Models A and D show isotropy/anisotropy due to geometry, and Model C has a single-crystalline-like texture but is isotropic and has low Young's modulus along the *x*-, *y*-, and *z*-axes. Model B was created to express anisotropy due to crystallographic texture, while Model E was created by superimposing anisotropy due to crystallographic textures on anisotropic shape. The <001> with the lowest Young's modulus is oriented in the direction with the lowest Young's modulus in terms of shape (*x*-axis), while the <011> with the higher Young's modulus is oriented in the direction with the highest Young's modulus in terms of shape (*z*-axis). Model F was intended to further increase the anisotropy in Young's modulus of the product by using <111> with the highest Young's modulus in *z*-axis.

The 3D puzzle samples fabricated are shown in Supplementary Fig. S6. The surface was polished to prepare for compression testing, and the powder in the unirradiated area was easily removed.

To confirm the crystallographic texture in the 3D puzzle products, EBSD analysis was performed in the center of the block indicated in black; the orientation information is shown in Fig. 6 as IPF maps and pole figures. Fabrication using ±XY_SS, ±X_SS, and +120°Rot_SS produced strong and preferentially oriented single-crystalline-like textures in the expected orientation <001>//BD, <011>//BD, and <111>//BD, respectively. However, these textures were not perfect single crystals (Fig. 6(b–d)). The specimen fabricated using ±67°Rot_SS exhibited a slightly elongated grain morphology in the oblique direction; the crystal orientation was highly randomized. The direction in which the grains elongated coincided with the direction in which the BD was projected. This is because the sample was produced with the diagonal parallel to the BD (Supplementary Fig. S4). Supplementary Fig. S7 was prepared to facilitate understanding in this regard.

Fig. 7 shows the Young's modulus analyzed along the three orthogonal axes of *x*, *y*, and *z* (or two axes of *x* and *z*) for each of the fabricated products. Color bars indicate measured values, and dashed lines indicate calculated values from Eqs. (1) to (2) using the moduli of single crystal

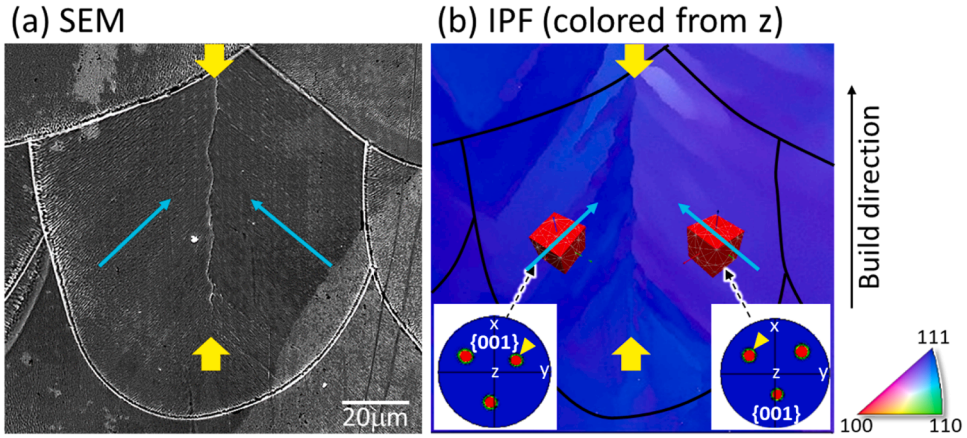

Fig. 4. (a) SEM micrograph and (b) the corresponding IPF map overlaid with the traces of the melt pool edges taken in a vertical cross-section of one melt pool. The IPF map is colored by the crystal orientation projected in the BD. Blue arrows indicate the direction of the long axis of the dendrite cross-section, which correspond to the projected direction of <001> onto this plane. Sets of facing yellow arrows indicate presence of fusion boundary.

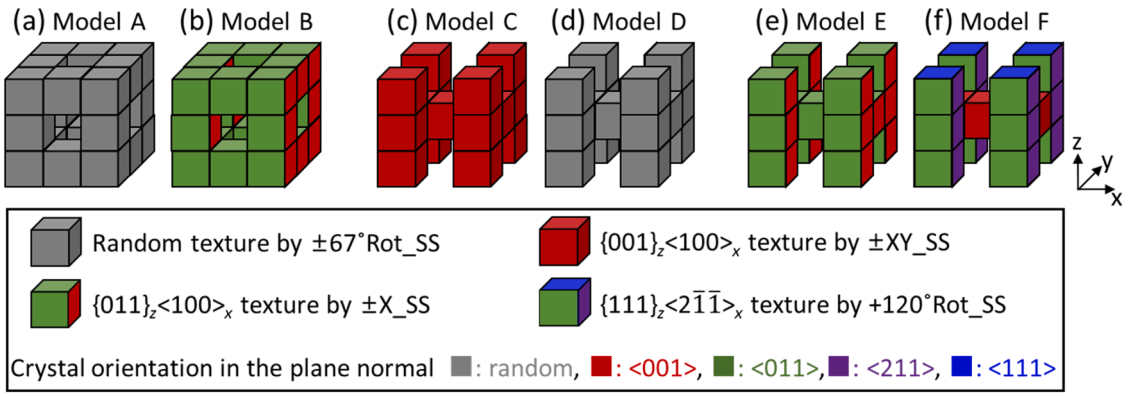

Fig. 5. 3D puzzle models proposed in this study in which four different crystallographic textures were superimposed on the two types of shape shown in Fig. 2(b). Crystallographic orientation preferentially oriented normal to the plane. The colors indicate the crystal planes that are preferentially oriented on each face.

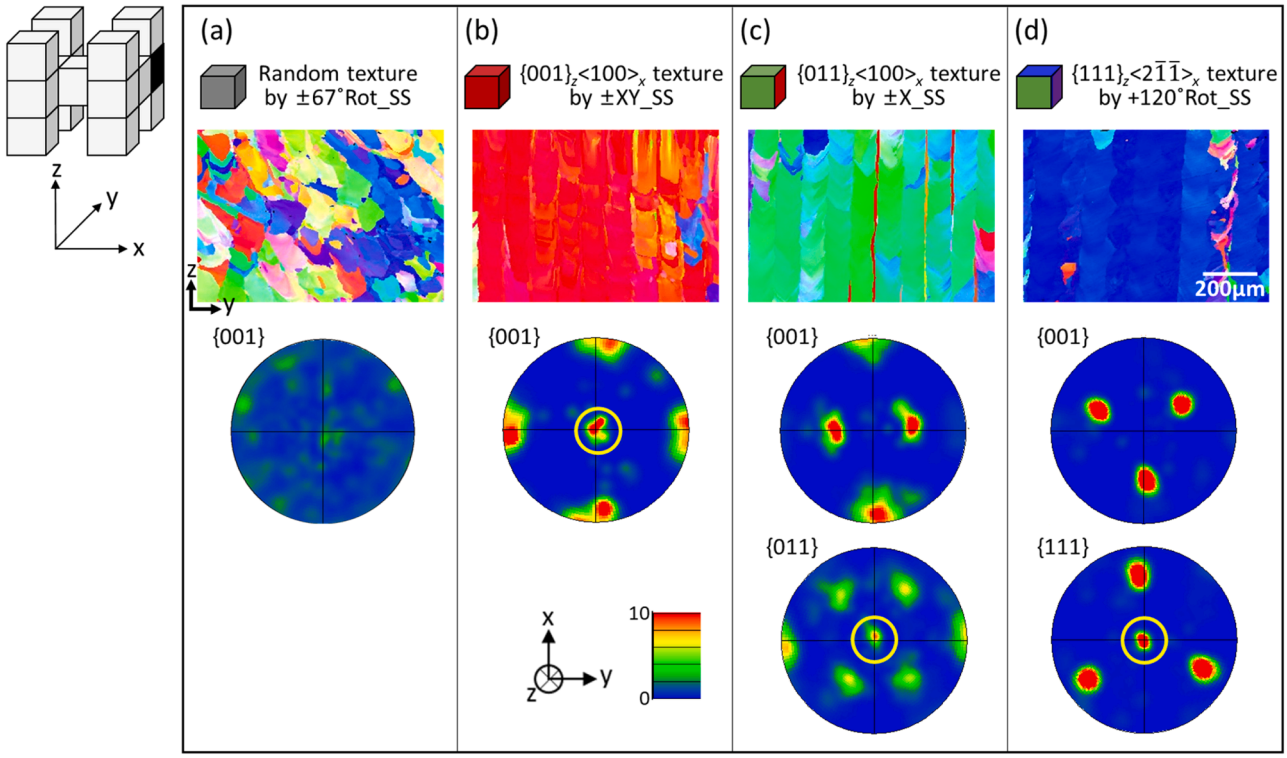

Fig. 6. IPF maps and pole figures indicating the crystallographic textures formed in 3D puzzle products. The data were taken in the center of the subelement indicated in black. The colors in the IPF map project the orientation in the *z*-axis.

as mentioned previously. Based on shape anisotropy and elastic anisotropy derived from crystallographic textures, Young's modulus anisotropy of the product was developed as hypothesized. In the polycrystalline (gray bars) and <011>-preferentially oriented directions (green bars), the measured values agreed well with the Young's modulus calculated from the single-crystal values. In contrast, the measured values were higher than the calculated values for the <001>-preferentially oriented direction (red bars) and were lower for the <111>-preferentially oriented direction (blue bar). The resulting anisotropy—defined as the ratio of the maximum to the minimum value of Young's modulus—was 1.03, 1.33, 3.52, 3.92, 5.38, and 5.86 for Models A–F, respectively. If a single crystal is formed in the 3D puzzle, the expected anisotropy would be 1.00, 1.91, 4.00, 4.00, 7.65, and 11.00, respectively.

5. Discussion

In this study, we proposed a product configuration that enables wide-range control of Young's modulus anisotropy of the product by superposition of shape anisotropy and crystallographic texture-based elastic anisotropy, and succeeded in demonstrating the expression of various degrees of anisotropy. In particular, the originality of this study is that, in addition to the previously realized <001>//BD and <011>//BD single-crystalline-like textures, we succeeded in obtaining <111>//BD single-crystalline-like texture by designing a new strategy and achieved anisotropy control through simultaneous shape and texture control. In this section, we discuss the mechanisms for the formation of single-crystalline-like textures, which are achieved only via unique production scheme in LPBF, from a scientific perspective, as well as the future prospects and limitations of this research.

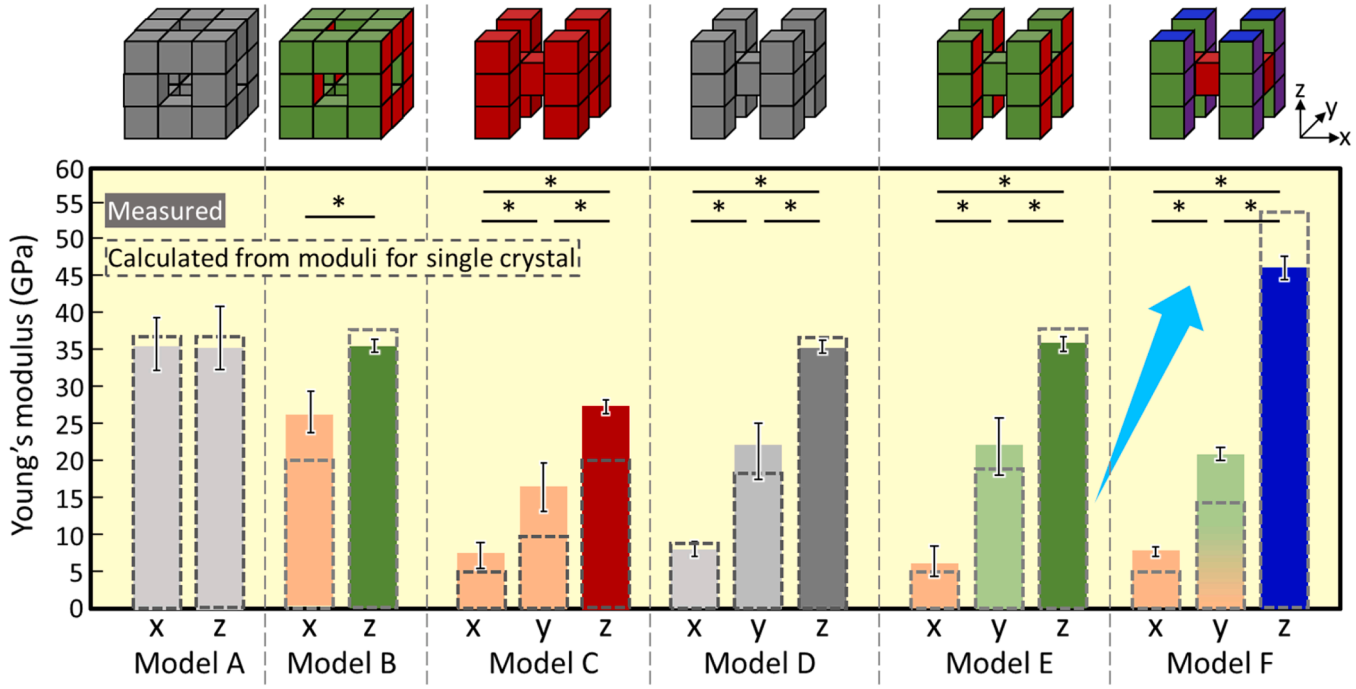

Fig. 7. Variation and anisotropy in the Young's modulus of the 3D puzzle products. Color bars indicate measured values, and dashed lines indicate calculated values using Reuss and Voigt laws and moduli for single crystal. *: $P < 0.05$.

5.1. Importance and difference between "bidirectional (±)" and "unidirectional (+)" laser scanning in terms of crystal orientation control

The key to realizing <111>/BD single-crystalline-like texture was the use of unidirectional (one-way) laser scanning, which had not been devised before, instead of the bidirectional scanning commonly practiced in LPBF manufacturing.

For successful formation of <001>//BD and <011>//BD single-crystalline-like textures, the laser must be scanned "bidirectionally" to localize <001> and <011> vertically upward (//BD). For metallic materials with relatively low to ordinary thermal conductivity, such as Ti-, Ni-, and Fe-based alloys, the melt pool has a long tail [3,27–29]; the tail is rather inclined toward the laser scanning direction. Accordingly, the heat flow direction would be tilted from the vertical downward direction (Fig. 8(a)) [3]. If the laser is scanned in only one direction (e.g., +*x*-direction), the crystal growth direction will have a component for scanning (*x*-) direction, which means that <001> or <011> is tilted away from the BD. By reciprocating the laser scanning (e.g., +*x*- and –*x*-directions) (Fig. 8(b)), the heat flow directions will have opposite tilts to each other on the *xz*-plane (Fig. 8(c)). However, despite some tilting of the heat flow direction, the crystal growth direction is self-adjusted between adjacent melt pool tracks (generated by +*x*- and –*x*-laser

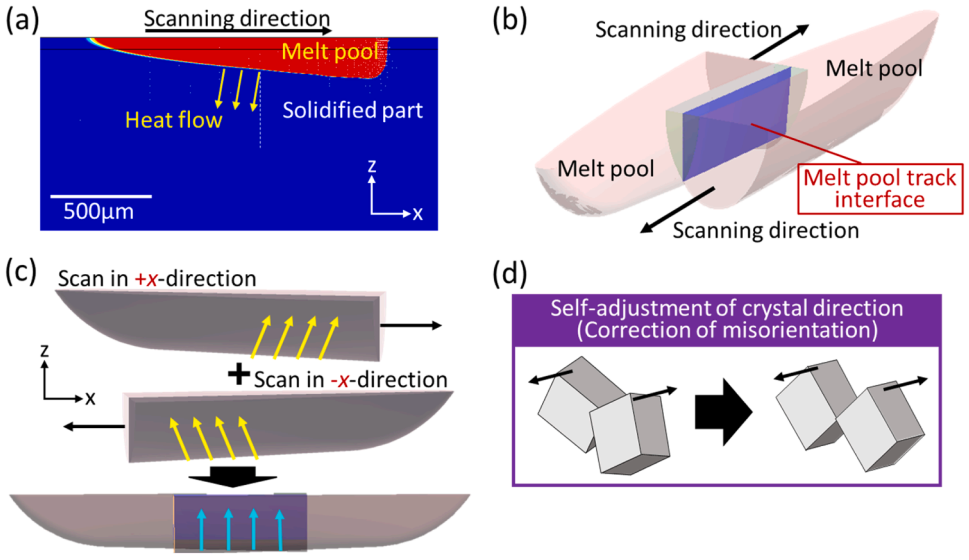

Fig. 8. Self-adjustment of crystal orientation by bidirectional laser scan via melt pool tract interface. (a) Long-tailed melt pool generated by laser scan and heat flow direction (arrows) due to the tilt of the melt pool bottom, simulated in Ti alloy (modified from Ref. [3]). (b) Illustration of the melt pool track interface formed by the bidirectional laser scan. (c) Schematic diagram of crystal growth direction tilted from vertical upward in the melt pool longitudinal section for +*x* scan and -*x* scan, respectively, and communization of crystal growth direction by bidirectional scan. (d) Self-adjustment of crystallographic orientation (correction of misorientation) between adjacent melt regions activated by bidirectional laser scan.

scanning), commoning to a vertical upward orientation, which results in identical crystal orientation between adjacent melt pool tracks (Fig. 8 (d)). This also implies that the crystal growth occurs substantially within the vertical cross-section of the melt pool (yellow plane in Fig. 9(d, e)). This self-adjustment could be driven by a decrease in crystallographic misorientation-derived interfacial energy at the adjacent melt-pool track interface (Fig. 8(b)).

Conversely, in the case of unidirectional scanning, self-adjustment of crystal growth direction does not occur within a solo layer, which itself should be the key to the <111>//BD single-crystalline-like texture formation. While the formation of <001>//BD and <011>//BD single-crystalline-like textures requires crystal growth in the vertical cross section of the melt pool (Fig. 9(d, e)), the formation of <111>//BD texture requires crystal growth within a section inclined in the scanning direction (Fig. 9(f)). The inclination from BD is 35.3°, which corresponds to the angle between <011> and <111> in cubic lattice. This is consistent with the fact that the oblique cross section of the <001>-elongated dendrite was observed (Fig. 4). This inclined plane in the melt pool (Fig. 9(f))—created by scanning from three directions at 120° intervals—forms three equivalent {001} planes, as shown in Fig. 1(f), which stabilizes the <111>//BD single-crystalline-like texture. In particular, <111>//BD single-crystalline-like texture can be obtained

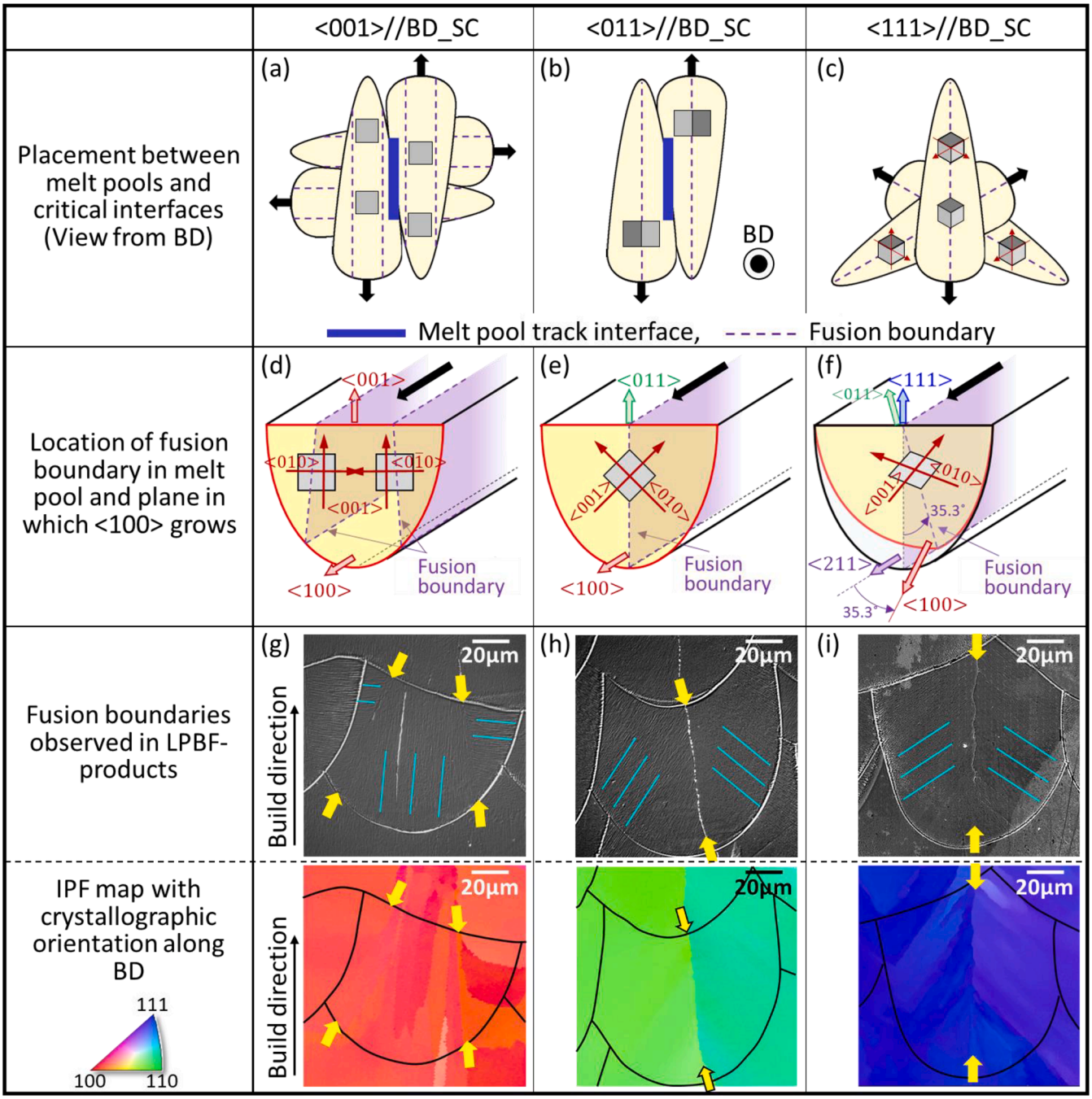

Fig. 9. Representation of fusion boundaries inside a melt pool, which contribute to the stabilization of crystal orientation. (a–c) Vertical and horizontal arrangements of melt pools as viewed from the BD. (d–f) Schematic of the location of fusion boundaries in a single melt pool. (g–i) Photograph of the vertical section of a single melt pool after etching and the corresponding IPF map in which crystal direction along the BD is represented. Sets of facing arrows indicate presence of fusion boundaries. The light blue lines indicate the direction of dendrite elongation.

only by utilizing this inclination, as opposed to correcting the heat flow inclination by using bidirectional scanning. In fact, using bidirectional scanning (i.e., ±120°R_SS), single-crystalline-like texture could not be obtained (Supplementary Fig. S8).

5.2. Role of "fusion boundary" of solidification fronts in a melt pool for stabilization of crystallographic orientation

As mentioned in the previous section, the formation of single-crystalline-like textures requires crystal growth to occur two-dimensionally in a specific plane within the melt pool. The specific plane is the vertical section of the melt pool for <001>//BD and <011>//BD textures, and the plane inclined 35.3° in the *x*-direction from the vertical section of the melt pool for <111>//BD texture. Within these planes, the crystal orientation is further self-adjusted owing to the presence of a "fusion boundary" formed in the melt pool (Fig. 9(d–f)). In the case of <011>//BD texture formation by ±X_SS, solidification fronts migrating from the right and left halves of the melt pool encounter at the melt pool center, forming a fusion boundary (Fig. 9(e, h)). In this case, the crystallographic misorientation in the left and right halves of the melt pool is aligned, which is driven by a decrease in crystallographic misorientation, and thus, the interfacial energy at the fusion boundary. Indeed, columnar dendrite structures that are inclined at approximately ±45° from the BD are observed in the left and right halves of the melt pool cross-section (Fig. 9(h)). The elongation direction of the dendrite corresponds to <001>. As a result, a single-crystalline-like texture with <011> preferential orientation to the BD was formed, leaving a slight angular difference at the fusion boundary. Although heat diffuses in the direction normal to the melt pool edge, the direction of the dendrites, i.e., the crystallographic orientation, is unity within each of the left and right halves of the melt pool. The inclined angle of the columnar dendrites of ±45° from BD is considered advantageous for the reduction of interfacial energy at the fusion boundary. Therefore, the crystal orientation is adjusted such that the crystallographic misorientation in the right and left halves of the melt pool reduces, leading to the ±45° dendrites from BD and <011>//BD orientation. Once the crystal orientation is stabilized, it is carried over to the upper layers by epitaxial growth.

In contrast, in the SS_XY, laser scans in the *x*- and *y*-directions intersect layer over layer, resulting in vertically upward and horizontal dendrite growths in the melt pool cross-section (Fig. 9(g)) to allow epitaxial growth in the layer immediately above. This is the result of self-adjustment of the crystal orientation in the three compartments in the melt pool to reduce misorientation at the two fusion boundaries in the melt pool (Fig. 9(d)). Accordingly, <001>//BD single-crystalline-like texture is formed.

In both cases, the mechanism involves self-adjustment of crystallographic orientation driven by reduction of crystallographic misorientation and, consequently, interfacial energy at the "fusion boundary." This mechanism is also true for +120°Rot_SS, which—similar to ±X_SS—forms a fusion boundary in the center of the melt pool (Fig. 9(i)) and stabilizes the crystal orientation in the direction that minimizes misorientation at the interface.

This reduction of misorientation at the fusion boundary is a common principle essential for single-crystal formation via LPBF with a long-tailed melt pool. Based on the crystal structure and preferential growth direction, single-crystalline texture will be obtained by appropriate selection of the combination of laser scanning directions and bidirectional/unidirectional mode, depending on the crystal direction to be oriented.

The resulting crystallographic orientation distribution in the three orthogonal directions of the formed texture is summarized in Fig. 10.

5.3. Scope for improvement in Young's modulus anisotropy

Young's moduli in the <001>- and <111>-orientated directions were higher and lower than the ideal value when assuming a single crystal, respectively (Fig. 7). The <001> direction exhibits the lowest Young's modulus, while the <111> direction exhibits the highest modulus. The deviation from the ideal values is caused by the imperfect crystal orientation. This leads to a reduction in Young's modulus anisotropy of the product, for example, in model F, Young's modulus anisotropy was reduced from 11.00 to 5.86. By further accentuating the crystal orientation, this anisotropy can be brought closer to the ideal value, and obtaining a crystallographic texture closer to a single crystal is a future challenge. A possible strategy to enhance the crystalline orientation is to fine-tune various process conditions. Exploring production with a high-power laser would be valuable, which was not feasible in this study due to equipment limitations. Preheating is another factor that affects the melt pool shape [30]. Moreover, gas flow, an integral part of the LPBF process, can reportedly disturb the texture [31]. Considering the present texture control methodology, where the laser SS (combination of laser scanning directions) is the key, the effects of single gas flow direction on melting by laser scanning in each direction cannot be homogenized. Elucidation of the effects of these factors and their optimization is essential to achieve a more prominent texture. Moreover, if the melt pool could be controlled to consist of flat surfaces perpendicular to the direction in which the <001> is desired to grow, the texture is expected to be more pronounced.

5.4. Toward generalization of single-crystalline-like texture control independent of alloys species and LPBF equipment

The mechanism for single-crystalline-like texture formation described in Sections 5.1 and 5.2 is applicable to other alloys that have cubic crystal structures and relatively low thermal conductivities. We successfully prepared three distinct single-crystalline-like textures in other alloys such as Ni-based superalloys and austenitic stainless steels. These findings will be detailed in separate papers. An important aspect is that the melt pool has a long tail, i.e., the slope at the melt pool bottom is moderately gentle. For <001>//BD and <011>//BD single-crystalline-like textures, the <001> growth direction in the melt-pool longitudinal

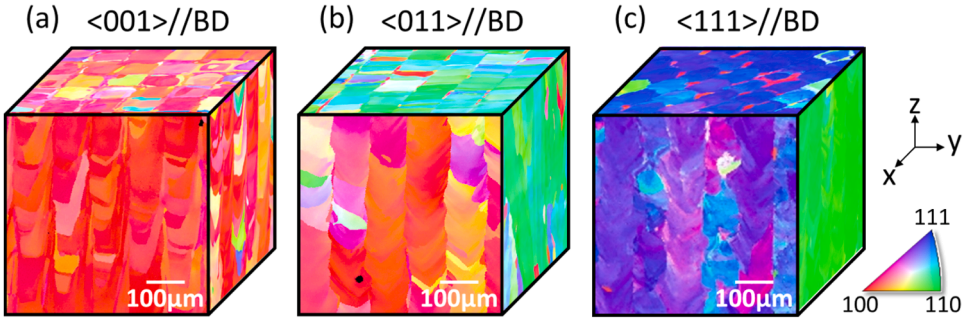

Fig. 10. Summary of crystallographic textures formed by each scanning strategy.

section must be adjusted vertically upward (BD) by the mechanism shown in Fig. 8, while for the <111>//BD texture, the <001> growth direction should be inclined to approximately 35.3° from the BD. Since the melt pool shape is determined by the balance between heat input and removal, the laser parameters must be adjusted depending on the laser absorption and thermal conductivity of the alloy to achieve similar single-crystalline-like texture formation. For this purpose, melt pool shape prediction using thermal or multiphysics simulation is useful. The laser conditions do not necessarily need to be the same for the fabrication of the three types of single-crystalline-like textures.

In addition, the device-independent generality of this texture control strategy must be discussed. The texture control strategy proposed in this study was designed based on crystal symmetry under the generation of appropriately shaped melt pools as described previously. Provided that the geometric similarity between the melt pool shape and the heat source scanning path is maintained, this strategy should be applicable even if the manufacturing device changes. In this study, a 100 μm-diameter laser was operated at a power of 360 W (near the upper limit of the EOS M 290 equipment). However, texture control under the same mechanism is possible in principle even with equipment having different laser configurations and spot sizes. Verification of this is an issue that should be explored in the future for investigating adaptability of the method across various setups.

In contrast, in materials with extremely high thermal conductivity, such as tungsten, the heat removal rate is large and the melt pool shows minimal tailing. In tungsten, a hemispherical melt pool is formed [3]. In that case, the heat flow direction is different from that of Ti alloy, and the three textures cannot be obtained with the strategy presented in this paper, although tungsten has a cubic crystal structure (BCC). Hence, further efforts are required to obtain texture variations in alloys with high thermal conductivity.

5.5. Future prospects for texture control via PBF

Several studies have reported the formation of fiber texture [21,32] and single-crystalline-like textures with <001>//BD and <011>//BD orientation [5,13,14,19–21]. In addition, other studies have successfully formed crystallographic lamellar microstructure (CLM) where <001>//BD- and <011>//BD-oriented layers were stacked alternately [2,33,34]. Arguably, many of these textures are controlled by the melt pool shape [33,35]. Deep melt pools promote <001> growth at ±45°, as explained above, forming a < 011>//BD orientation. If the curvature of the melt pool bottom is large, a layer of <001>//BD orientation forms originating from the center of the melt pool bottom, contributing to the formation of the CLM [2,33,34]. Shallow melt pools promote <001> growth parallel to BD, forming <001>//BD orientation [5]. The extremely small hatch spacing unifies the heat flow direction to one inclined direction from the BD, providing a texture where the <001> is inclined from the BD [33]. Therefore, efforts are being made to change the melt pool shape to modify the texture [31,35–37]. However, this approach did not yield <111>//BD-oriented single crystals. In this study, a complete set of three different single-crystal-like textures—<001>//BD, <011>//BD, and <111>//BD—was achieved via a new strategy of aligning the scanning direction of the heat source with the symmetry of the crystal (including the choice of round-trip or one-way), rather than the melt pool shape control. The laser irradiation conditions (laser power, scanning speed, layer thickness, and hatch spacing) were the same for the three SSs in this study, thus, the melt pool shapes are approximately equal. The design of SSs based on crystal symmetry has not been studied previously and provides important insights into texture control with PBF.

5.6. Anticipated impact on advancements in component design and manufacturing

The ability to produce components with various crystal orientations reported in this study is expected to be groundbreaking for conventional component design guidelines. In particular, the conventional design method using computer-aided design (CAD), which defines only the shape of the component, will evolve into a new design method that includes SSs defined for each location inside the component. As a result, the anisotropy of the mechanical properties of each location can be incorporated within the component as a design guideline, which is expected to revolutionize the conventional component design methodology. Topology optimization, in which 3D printing originally excels [38], will lead to the simultaneous optimization of topology and internal structure. This advancement not only expands the range of controllable functions but also contributes to achieving higher mechanical properties limits, leading to further weight reduction without compromising performance. While recent multi-material topology optimization (MMTO) can use heterogeneous materials with different Young's moduli (assuming polycrystals with isotropic Young's modulus) and simultaneously optimize their arrangement and shape [39,40], in the new design strategy proposed in this study, optimization similar to MMTO is possible by utilizing the anisotropy of a single material.

Fig. 11 illustrates two representations of the mechanical functionalization of products: the suspension arm as a mechanical component and the hip implant as a biomedical device, through superimposed control of shape and internal texture, as proposed in this study. Topology optimization and/or shape customization are the well-documented advantages of conventional AM. However, the local stress concentration, which is unavoidable, can be alleviated by increasing stiffness through the control of crystal orientation, and severe strain shielding of the bone in the case of bone devices can be alleviated by decreasing stiffness. Furthermore, if the required strength properties are different for different parts of the product, the SS can be adjusted for each part to provide the required crystal orientation and strength properties (Fig. 12). The findings of this study provide new insights into component design methodology that incorporates scanning strategies (information on the orientation to be created) into the 3D model, rather than designing only the shape in CAD.

6. Conclusion

In this study, we explored the mechanism behind single-crystal formation by LPBF and proposed a novel heat-source scan strategy to achieve <111>//BD-oriented single crystal, which has not been previously demonstrated. We succeeded in forming <111>//BD-oriented single-crystal-like texture for the first time, and completed three types of single crystals with <001>, <011>, and <111>//BD orientations. As a result, by utilizing the <001> orientation for the lowest Young's modulus and the <111> orientation for the highest Young's modulus, we developed a framework for fabricating products with extremely large Young's modulus anisotropy.

The formation of single crystals is governed by the self-adjustment of crystal orientation, which minimizes crystallographic misorientation and, consequently, interface energy. This adjustment occurs at both the melt-pool truck interface formed by reciprocal scanning and at the fusion boundary where solid–liquid interfaces meet in the melt pool. This mechanism provides an insight into the control of crystallographic texture by PBF and can be applied to materials that exhibit different crystal structures and/or crystal growth directions.

Finally, the achievements of this study could be definitive to component design guidelines. In particular, superimposing the design of compartment-dependent crystallographic textures on conventional shape optimization represents a novel strategy for product mechanical design, achievable only through AM.

CRediT authorship contribution statement

Takuya Ishimoto: Writing – review & editing, Writing – original draft, Validation, Methodology, Conceptualization. **Naotaka Morita:**

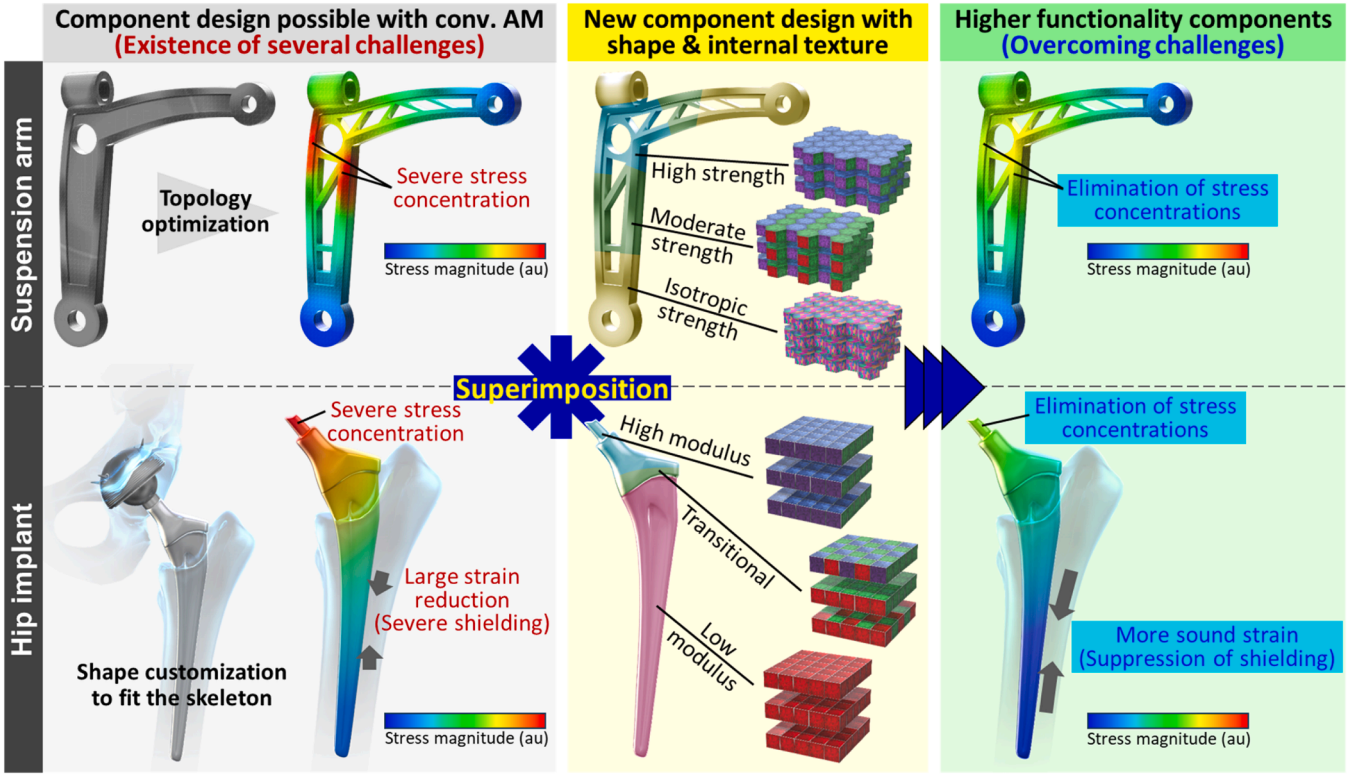

Fig. 11. Conceptual diagram of high mechanical functionalization of products by superposition of shape control and internal texture control proposed in this study. A suspension arm as a mechanical component and a hip implant as a medical device are shown as examples.

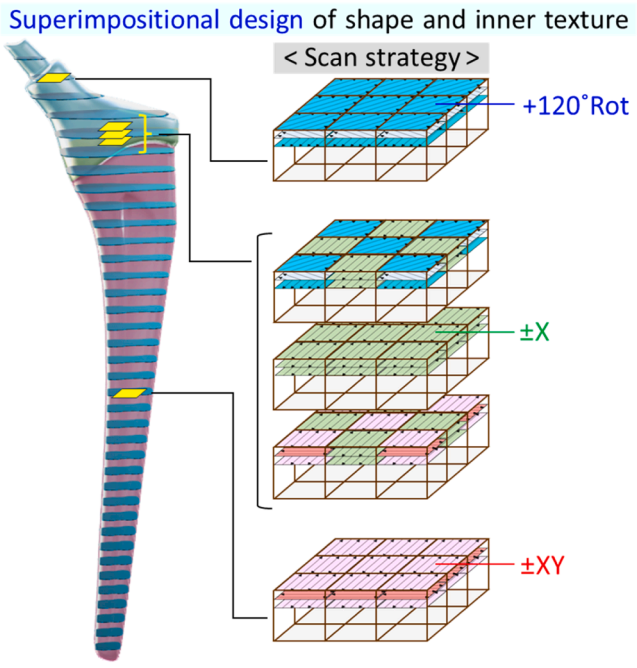

Fig. 12. Schematic of a 3D model encompassing scanning strategies to obtain the required properties (texture) for each part.

Visualization, Validation, Methodology, Investigation, Data curation. **Ryosuke Ozasa:** Writing – review & editing, Investigation. **Aira Matsugaki:** Writing – review & editing, Investigation. **Ozkan Gokcekaya:** Writing – review & editing, Investigation. **Shota Higashino:** Writing – review & editing, Investigation. **Masakazu Tane:** Supervision, Investigation. **Tsuyoshi Mayama:** Writing – review & editing, Investigation. **Ken Cho:** Writing – review & editing, Investigation. **Hiroyuki Y. Yasuda:** Supervision, Investigation. **Masayuki Okugawa:** Writing – review & editing, Investigation. **Yuichiro Koizumi:** Supervision, Investigation. **Masato Yoshiya:** Supervision, Investigation. **Daisuke Egusa:** Writing – review & editing, Investigation. **Taisuke Sasaki:** Writing – review & editing, Investigation. **Eiji Abe:** Supervision, Investigation. **Hajime Kimizuka:** Supervision, Investigation. **Naoko Ikeo:** Writing – review & editing, Investigation. **Takayoshi Nakano:** Writing – review & editing, Validation, Supervision, Project administration, Funding acquisition, Conceptualization.

Declaration of competing interest

The authors declare that they have no known competing financial interests or personal relationships that could have influenced the work reported in this paper.

Acknowledgments

This work was supported by CREST-Nanomechanics: Elucidation of macroscale mechanical properties based on understanding nanoscale dynamics for innovative mechanical materials (Grant Number: JPMJCR2194) from the Japan Science and Technology Agency (JST).

Supplementary materials

Supplementary material associated with this article can be found, in the online version, at doi:10.1016/j.actamat.2025.120709.

Data availability

Data will be made available on request.

References

[1] K. Kanishka, B. Acherjee, Revolutionizing manufacturing: a comprehensive overview of additive manufacturing processes, materials, developments, and challenges, J. Manuf. Proc. 107 (2023) 574–619, https://doi.org/10.1016/j.jmapro.2023.10.024.

[2] O. Gokcekaya, T. Ishimoto, S. Hibino, J. Yasutomi, T. Narushima, T. Nakano, Unique crystallographic texture formation in Inconel 718 by laser powder bed fusion and its effect on mechanical anisotropy, Acta Mater. 212 (2021) 116876, https://doi.org/10.1016/j.actamat.2021.116876.

[3] T. Todo, T. Ishimoto, O. Gokcekaya, J. Oh, T. Nakano, Single crystalline-like crystallographic texture formation of pure tungsten through laser powder bed fusion, Scr. Mater. 206 (2022) 114252, https://doi.org/10.1016/j.scriptamat.2021.114252.

[4] Z. Sun, X. Tan, S.B. Tor, C.K. Chua, Simultaneously enhanced strength and ductility for 3D-printed stainless steel 316L by selective laser melting, NPG Asia Mater. 10 (2018) 127–136, https://doi.org/10.1038/s41427-018-0018-5.

[5] S.H. Sun, K. Hagihara, T. Ishimoto, R. Suganuma, Y.F. Xue, T. Nakano, Comparison of microstructure, crystallographic texture, and mechanical properties in Ti–15Mo–5Zr–3Al alloys fabricated via electron and laser beam powder bed fusion technologies, Addit. Manuf. 47 (2021) 102329, https://doi.org/10.1016/j.addma.2021.102329.

[6] T. Ishimoto, R. Suganuma, T. Nakano, Tailoring the crystallographic texture of biomedical metastable β-type Ti-alloy produced via laser powder bed fusion using temperature-field simulations, Mater. Lett. 349 (2023) 134835, https://doi.org/10.1016/j.matlet.2023.134835.

[7] L. Xue, K.C. Atli, C. Zhang, N. Hite, A. Srivastava, A.C. Leff, A.A. Wilson, D. J. Sharar, A. Elwany, R. Arroyave, I. Karaman, Laser powder bed fusion of defect-free NiTi shape memory alloy parts with superior tensile superelasticity, Acta Mater. 229 (2022) 117781, https://doi.org/10.1016/j.actamat.2022.117781.

[8] B.B. Zhang, Y.G. Tang, Q.S. Mei, X.Y. Li, K. Lu, Inhibiting creep in nanograined alloys with stable grain boundary networks, Science 378 (2022) 659–663, https://doi.org/10.1126/science.abq7739 (1979).

[9] M. Tane, S. Akita, T. Nakano, K. Hagihara, Y. Umakoshi, M. Niinomi, H. Nakajima, Peculiar elastic behavior of Ti-Nb-Ta-Zr single crystals, Acta Mater. 56 (2008) 2856–2863, https://doi.org/10.1016/j.actamat.2008.02.017.

[10] S.H. Lee, M. Todai, M. Tane, K. Hagihara, H. Nakajima, T. Nakano, Biocompatible low Young's modulus achieved by strong crystallographic elastic anisotropy in Ti-15Mo-5Zr-3Al alloy single crystal, J. Mech. Behav. Biomed. Mater. 14 (2012) 48–54, https://doi.org/10.1016/j.jmbbm.2012.05.005.

[11] K. Hagihara, T. Nakano, Experimental clarification of the cyclic deformation mechanisms of β-type Ti–Nb–Ta–Zr-alloy single crystals developed for the single-crystalline implant, Int. J. Plast. 98 (2017) 27–44, https://doi.org/10.1016/j.ijplas.2017.06.006.

[12] R. Huiskes, H. Weinans, B. van Rietbergen, The relationship between stress shielding and bone resorption around total hip stems and the effects of flexible materials, Clin. Orthop. Relat. Res. 274 (1992) 124–134, https://doi.org/10.1097/00003086-199201000-00014.

[13] T. Ishimoto, K. Hagihara, K. Hisamoto, S.H. Sun, T. Nakano, Crystallographic texture control of beta-type Ti-15Mo-5Zr-3Al alloy by selective laser melting for the development of novel implants with a biocompatible low Young's modulus, Scr. Mater. 132 (2017) 34–38, https://doi.org/10.1016/j.scriptamat.2016.12.038.

[14] S.H. Sun, K. Hagihara, T. Nakano, Effect of scanning strategy on texture formation in Ni-25 at.%Mo alloys fabricated by selective laser melting, Mater. Des. 140 (2018) 307–316, https://doi.org/10.1016/j.matdes.2017.11.060.

[15] Y. Zhong, R. An, H. Ma, C. Wang, Low-temperature-solderable intermetallic nanoparticles for 3D printable flexible electronics, Acta Mater. 162 (2019) 163–175, https://doi.org/10.1016/j.actamat.2018.09.069.

[16] X. Luan, H. Qin, F. Liu, Z. Dai, Y. Yi, Q. Li, The mechanical properties and elastic anisotropies of cubic Ni_3Al from first principles calculations, Crystals (Basel) 8 (2018) 307, https://doi.org/10.3390/cryst8080307.

[17] C. Kumara, D. Deng, J. Moverare, P. Nylén, Modelling of anisotropic elastic properties in alloy 718 built by electron beam melting, Mater. Sci. Technol. 34 (2018) 529–537, https://doi.org/10.1080/02670836.2018.1426258.

[18] A. Basavalingappa, M.Y. Shen, J.R. Lloyd, Modeling the copper microstructure and elastic anisotropy and studying its impact on reliability in nanoscale interconnects, Mech. Adv. Mater. Mod. Proc. 3 (2017) 6, https://doi.org/10.1186/s40759-017-0021-5.

[19] X. Qi, X. Liang, J. Wang, H. Zhang, X. Wang, Z. Liu, Microstructure tailoring in laser powder bed fusion (L-PBF): strategies, challenges, and future outlooks, J. Alloys Compd. 970 (2024) 172564, https://doi.org/10.1016/j.jallcom.2023.172564.

[20] K. Hagihara, T. Nakano, Control of anisotropic crystallographic texture in powder bed fusion additive manufacturing of metals and ceramics—A review, JOM 74 (2022) 1760–1773, https://doi.org/10.1007/s11837-021-04966-7.

[21] J.J. Marattukalam, D. Karlsson, V. Pacheco, P. Beran, U. Wiklund, U. Jansson, B. Hjörvarsson, M. Sahlberg, The effect of laser scanning strategies on texture, mechanical properties, and site-specific grain orientation in selective laser melted 316L SS, Mater. Des. 193 (2020) 108852, https://doi.org/10.1016/j.matdes.2020.108852.

[22] R.W. Messler, Principles of Welding, Wiley, New York, 2008.

[23] S. Patel, M. Vlasea, Melting modes in laser powder bed fusion, Materialia (Oxf) 9 (2020) 100591, https://doi.org/10.1016/j.mtla.2020.100591.

[24] N. Ikeo, H. Fukuda, A. Matsugaki, T. Inoue, A. Serizawa, T. Matsuzaka, T. Ishimoto, R. Ozasa, O. Gokcekaya, T. Nakano, 3D puzzle in cube pattern for anisotropic/isotropic mechanical control of structure fabricated by metal additive manufacturing, Crystals (Basel) 11 (2021) 959, https://doi.org/10.3390/cryst11080959.

[25] G. Yamamoto, Y. Sakuda, Determination of elastic constants in complex-shaped materials through vibration-mode-pattern-matching-assisted resonant ultrasound spectroscopy, J. Appl. Phys. 135 (2024) 205109, https://doi.org/10.1063/5.0185423.

[26] M. Rappaz, J.A. Dantzig, Solidification, 2nd ed., EFPL Press, Lausanne, 2016.

[27] T.N. Le, Y.L. Lo, Z.H. Lin, Numerical simulation and experimental validation of melting and solidification process in selective laser melting of IN718 alloy, Addit. Manuf. 36 (2020) 101519, https://doi.org/10.1016/j.addma.2020.101519.

[28] M.J. Ansari, D.S. Nguyen, H.S. Park, Investigation of SLM process in terms of temperature distribution and melting pool size: modeling and experimental approaches, Materials (Basel) 12 (2019) 1272, https://doi.org/10.3390/ma12081272.

[29] M.S. Pham, B. Dovgyy, P.A. Hooper, C.M. Gourlay, A. Piglione, The role of side-branching in microstructure development in laser powder-bed fusion, Nat. Commun. 11 (2020) 749, https://doi.org/10.1038/s41467-020-14453-3.

[30] Q. Chen, Y. Zhao, S. Strayer, Y. Zhao, K. Aoyagi, Y. Koizumi, A. Chiba, W. Xiong, A. C. To, Elucidating the effect of preheating temperature on melt pool morphology variation in Inconel 718 laser powder bed fusion via simulation and experiment, Addit. Manuf. 37 (2021) 101642, https://doi.org/10.1016/j.addma.2020.101642.

[31] H. Amano, T. Ishimoto, K. Hagihara, R. Suganuma, K. Aiba, S.H. Sun, P. Wang, T. Nakano, Impact of gas flow direction on the crystallographic texture evolution in laser beam powder bed fusion, Virtual Phys. Prototyp. 18 (2023) e2169172, https://doi.org/10.1080/17452759.2023.2169172.

[32] A. Fardan, U. Klement, H. Brodin, E. Hryha, Effect of part thickness and build angle on the microstructure, surface roughness, and mechanical properties of additively manufactured IN-939, Metal. Mater. Trans. A 54 (2023) 1792–1807, https://doi.org/10.1007/s11661-022-06940-7.

[33] A. Thomas, G. Fribourg, J.J. Blandin, P. Lhuissier, R. Dendievel, G. Martin, Tailoring the crystallographic texture of pure copper through control of the scanning strategy in electron powder bed fusion, Materialia (Oxf) 24 (2022) 101495, https://doi.org/10.1016/j.mtla.2022.101495.

[34] S.H. Sun, T. Ishimoto, K. Hagihara, Y. Tsutsumi, T. Hanawa, T. Nakano, Excellent mechanical and corrosion properties of austenitic stainless steel with a unique crystallographic lamellar microstructure via selective laser melting, Scr. Mater. 159 (2019) 89–93, https://doi.org/10.1016/j.scriptamat.2018.09.017.

[35] O. Andreau, I. Koutiri, P. Peyre, J.D. Penot, N. Saintier, E. Pessard, T. De Terris, C. Dupuy, T. Baudin, Texture control of 316L parts by modulation of the melt pool morphology in selective laser melting, J. Mater. Process. Technol. 264 (2019) 21–31, https://doi.org/10.1016/j.jmatprotec.2018.08.049.

[36] D.E. Jodi, T. Kitashima, Y. Koizumi, T. Nakano, M. Watanabe, Manufacturing single crystals of pure nickel via selective laser melting with a flattop laser beam, Addit. Manuf. Lett. 3 (2022) 100066, https://doi.org/10.1016/j.addlet.2022.100066.

[37] J. Bi, L. Wu, S. Li, Z. Yang, X. Jia, M.D. Starostenkov, G. Dong, Beam shaping technology and its application in metal laser additive manufacturing: a review, J. Mater. Res. Technol. 26 (2023) 4606–4628, https://doi.org/10.1016/j.jmrt.2023.08.037.

[38] O. Ibhadode, Z. Zhang, J. Sixt, K.M. Nsiempba, J. Orakwe, A. Martinez-Marchese, O. Ero, S.I. Shahabad, A. Bonakdar, E. Toyserkani, Topology optimization for metal additive manufacturing: current trends, challenges, and future outlook, Virtual Phys. Prototyp. 18 (2023) e2181192, https://doi.org/10.1080/17452759.2023.2181192.

[39] B. Yi, G.H. Yoon, R. Zheng, L. Liu, D. Li, X. Peng, A unified material interpolation for topology optimization of multi-materials, Comput. Struct. 282 (2023) 107041, https://doi.org/10.1016/j.compstruc.2023.107041.

[40] F.M. Conde, P.G. Coelho, J.M. Guedes, Multi-scale topology optimization of structures with multi-material microstructures using stiffness and mass design criteria, Adv. Eng. Softw. 187 (2024) 103566, https://doi.org/10.1016/j.advengsoft.2023.103566.